The radio signal of PSR B0950 + 08 is detected over the whole pulse phase

Zhengli Wang,[1] Jiguang Lu [ORCID],[2,3]★ Jinchen Jiang [ORCID],[4] Jie Lin,[4] Kejia Lee,[4,5] Enwei Liang[1] and Renxin Xu [ORCID][4,5]★

[1]*Guangxi Key Laboratory for Relativistic Astrophysics, School of Physical Science and Technology, Guangxi University, Nanning 530004, China*
[2]*National Astronomical Observatories, Chinese Academy of Sciences, Beijing 100012, China*
[3]*Guizhou Radio Astronomical Observatory, Guizhou 550025, China*
[4]*Department of Astronomy, School of Physics, Peking University, Beijing 100871, China*
[5]*Kavli Institute for Astronomy and Astrophysics, Peking University, Beijing 100871, China*

ABSTRACT

Pulsars are known as the 'lighthouses' of the Universe. Periodic pulses with a duty cycle of ~ 10 per cent are detected when the radio beam of a rotating pulsar sweeps across the telescope. In this report, 160-min data of a nearby pulsar, PSR B0950 + 08, observed with the Five-hundred-meter Aperture Spherical radio Telescope (FAST) are analysed. Thanks to the extremely high sensitivity of FAST, it is found that the radiation of PSR B0950 + 08 can be detected over the entire pulse period. To investigate the radiative characteristics of the pulsar's 'bridge emission', a function, $\Theta(n)$, is defined to reveal the weak radiation there. It is suggested that the narrow peaks of both the main pulses and interpulses could be radiated at low altitude, while other weak emission (e.g. the 'bridges') comes from the upper magnetosphere, though its radiative mechanism is still a matter of debate. The measured mean pulse behaviours are consistent with previous results in the phase of strong emission of this pulsar, and both the frequency-independent separation between the interpulse and main pulse and the narrow pulse width may support a double-pole model. In order to understand the magnetospheric geometry of this pulsar, further polarization-calibrated observation with FAST and a proper determination of the baseline emission, especially during the weak emission phase, are surely required.

Key words: pulsars: general – pulsars: individual: PSR B0950 + 08 – radio continuum: stars.

1 INTRODUCTION

The nearby, bright pulsar PSR B0950 + 08 is well known, with a spin period of 253 ms and dispersion measure (DM) of 2.97 pc cm^{-3}. Abundant observations have already been obtained for this normal pulsar (e.g. Hankins et al. 1991; Kuzmin et al. 1998; Everett & Weisberg 2001; Shabanova & Shitov 2004; Johnston et al. 2005). For instance, the averaged pulse profile of PSR B0950 + 08 shows frequency-dependent properties (e.g. Hankins et al. 1991; Kuzmin et al. 1998), and Shabanova & Shitov (2004) reported that the frequency-dependent sinusoidal modulation of the pulse shape may result from the Faraday rotation effect. Also, its linear polarization is shown in the literature (e.g. Everett & Weisberg 2001; Shabanova & Shitov 2004; Johnston et al. 2005), but is too low to fit the polarization position angle (PPA) at the main pulse longitude with a typical 'S' shape in the rotating vector model (RVM: Radhakrishnan & Cooke 1969). In fact, Everett & Weisberg (2001) presented the RVM fitting for PSR B0950 + 08. When they fitted the PPA of the whole pulse longitudes (Fig. 8), the longitude range $(-10, +15)°$ of distortion regions appearing in the main pulse must be unweighted. Popov et al. (2002) confirmed that the characteristic time-scales of microstructure and narrow microstructure are of order 0.1 ms and 10 μs, respectively, while the time-scale of fine structure is $\sim$1 ms (Ulyanov et al.

2016). Also, the separation between the interpulse and main pulse is frequency-independent below 5 GHz, and this feature demonstrates that a multipole magnetic field may contribute significantly, in order to understand the 'bridge' emission (Hankins & Cordes 1981; Nowakowski, Bhat & Lorimer 2002).

In addition to the mean pulse profile, single-pulse behaviours have been studied for PSR B0950 + 08. After a detailed study of the intensity dependence of individual pulses, Nowakowski et al. (2002) found a possible correlation between the intensities and locations of the interpulse and the leading component of the main pulse. Additionally, PSR B0950 + 08 also exhibits the nulling pulse phenomenon and sharp flux variation in a short-time scale (e.g. Cairns 2004; Shabanova & Shitov 2004; Singal & Vats 2012). Also, giant pulse and giant micropulse phenomena have also been detected from PSR B0950 + 08 (e.g. Cairns 2004; Singal & Vats 2012; Tsai et al. 2015), but their origin is still a mystery.

Nevertheless, properties of both the mean pulse and single pulses will be influenced significantly by the baseline determination. Conventional baseline subtraction is to subtract the weak emission region from the strong emission phase (i.e. the main pulse) of the pulsar. If this baseline subtraction is used directly to subtract the weak emission region of a pulsar with unusually wide pulse, such as PSR B0950 + 08, the impulsive radio signal of the weak emission phase of this pulsar is also subtracted. More details on discussion of the baseline will be presented in a later section of this work. Hankins & Cordes (1981) strongly supported the conclusion that the

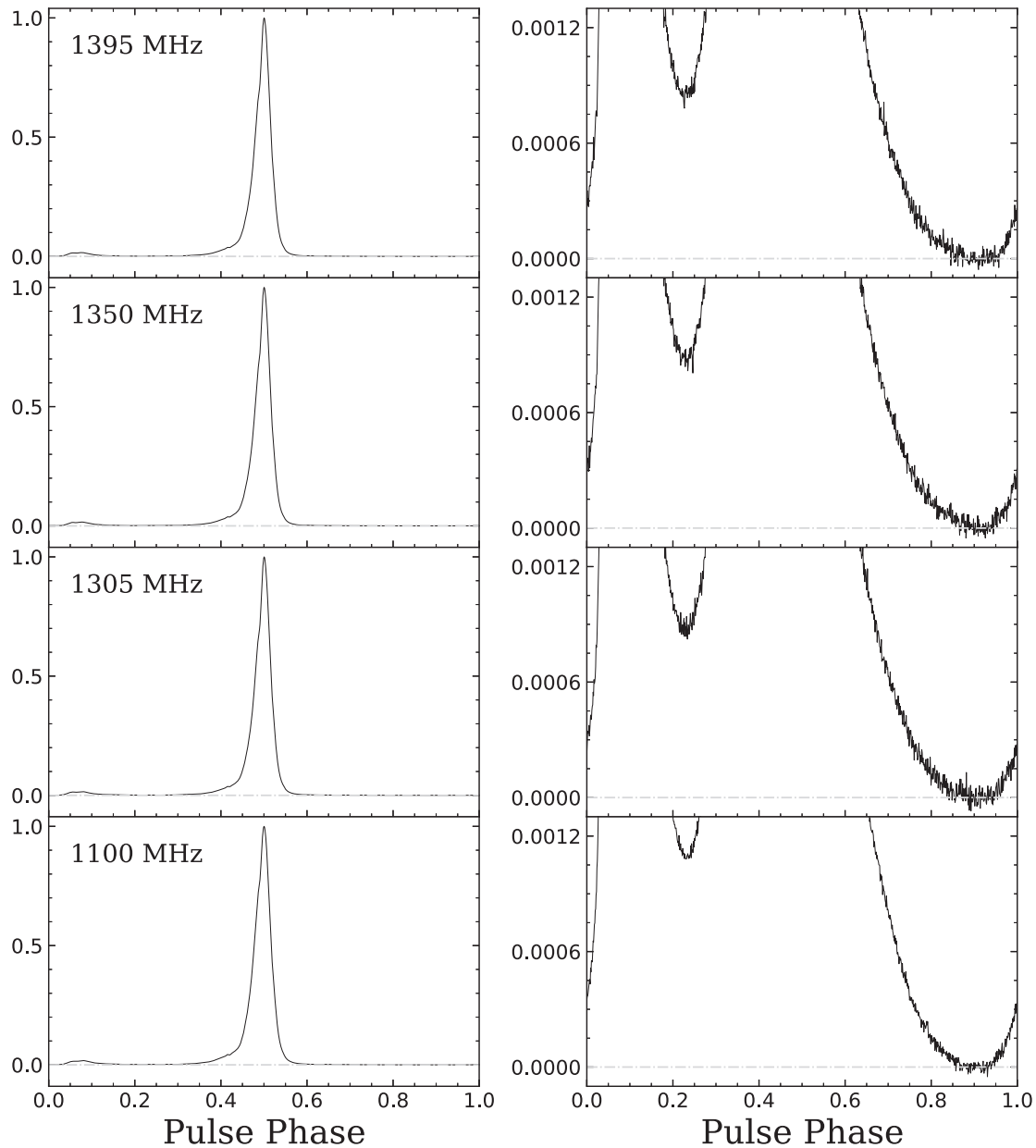★ E-mail: lujig@pku.edu.cn (JL); r.x.xu@pku.edu.cn (RX)

Figure 1. The averaged pulse profiles at 1100, 1305, 1350, and 1395 MHz are shown in the left panel, and the corresponding ×800 expanded scale views are plotted in the right panels. The emission region of the pulse phase from 0.88–0.92 is regarded as the baseline region.

radio emission from PSR B0950 + 08 occurs over at least 83 per cent of the rotation period. They pointed out that, because of limited sensitivity of telescopes, the radio emission character of the 'two minimum levels' at the bridge regions between the interpulse and main pulse (the remaining 17 per cent pulse longitude) could not be defined with certainty.

Up to now, similar properties have also been discovered in PSR B1929 + 10 and some other millisecond pulsars (e.g. McLaughlin & Rankin 2004; Dai et al. 2015); for all these pulsars it has been reported that the emission covers an unusually wide range of pulse longitude. Therefore, the radio emission of the whole pulse phase for these pulsars is worth detecting. Navarro et al. (1995) discovered a binary millisecond pulsar, PSR J0218 + 4232, with an extremely broad pulse profile during imaging observations; they later confirmed that

this pulsar exhibits a significant fraction of radio emission that is not pulsed. Meanwhile, Ruan et al. (2020) reported a detection result of the emission features of off-pulse emission (the emission is non-periodic and stationary) from PSR B0950 + 08. Through imaging analysis, they concluded that the off-pulse emission of this pulsar originates mainly from outside the magnetosphere. Nevertheless, it is hard to rule out completely the possibility of a magnetospheric origin for off-pulse emission via imaging. The difference between emission origins from inside and outside the magnetosphere is whether the radiation is impulsive and periodic, and in this work we attempt to detect the impulsive characteristic of PSR B0950 + 08. However, not all radio pulsars have off-pulse emission, Marcote et al. (2019) presented a detailed detection of off-pulse emission for B0525 + 21 and B2045 − 16. They reported that off-pulse emission above three

times the rms noise levels for B0525 + 21 and B2045 − 16 is not detected using the European Very-Long-Baseline Interferometry (VLBI) Network. The imaging method could potentially be used to determine pulsars with wide pulse profile such as PSR B1929 + 10 in the future.

The largest single-dish radio telescope in the world, China's Five-hundred-meter Aperture Spherical radio Telescope (FAST), would be an appropriate tool to understand more about radio emission as well as the radiative mechanism of PSR B0950 + 08, taking advantage of its extremely high sensitivity (Jiang et al. 2019, 2020). New scientific achievements have already been obtained with FAST, including studies of pulsars (e.g. Lu et al. 2019) and fast radio bursts (e.g. Xu 2021). In this work, the emission from the 'bridge' of PSR B0950 + 08 is determined (as shown in Fig. 1), exhibiting a concave structure. A detailed study of the radiation properties of the entire 360° pulse longitude is presented. The observations with FAST and the data reduction are described in Section 2. To determine the emission for the entire pulse period, an in-depth data analysis and the radiation characteristics of this pulsar are presented in Section 3. Finally, a general conclusion and discussion are provided in Section 4.

2 OBSERVATION AND DATA REDUCTION

FAST is located in Guizhou, a southwestern province of China, at longitude 106.9° E and latitude 25.7° N. In this work, the 19-beam receiver system was adopted. The central frequency and bandwidth of the receiver are 1250 and 400 MHz, respectively (Jiang et al. 2019, 2020). The system temperature of the 19-beam receiver is less than 24 K for the central beam, and the system stability for most observation modes with observation zenith angle less than 26.4° is ∼ 1 per cent over 3.5 hours (Jiang et al. 2019, 2020)

In this work, PSR B0950 + 08 was observed with tracking mode on MJD 59396 (2021 July 1). The data were recorded in the 8-bit-sampled search mode PSRFITS format (Hotan, van Straten & Manchester 2004) with 4096 frequency channels, and the frequency resolution is ∼ 0.122 MHz. The entire integration time is 160 minutes and the time resolution is ∼ 50 μs. The DSPSR software package (van Straten & Bailes 2011) was adopted in the data reduction, and the individual pulses were generated with 1024 phase bins across the pulse period of 253 ms (Hobbs et al. 2004).

To ensure that the radio signal of the weak emission region of PSR B0950 + 08 is not affected by radio frequency interference (RFI), the RFI is detected using the dynamic spectrum. Significant and possible impulsive RFIs are eliminated. Moreover, the narrow-band RFI is also mitigated efficiently by using the dynamics spectrum. Then only the integrated sub-band data with frequencies of 1100, 1305, 1350, and 1395 MHz remain, and their bandwidths are 80, 50, 40, and 50 MHz, respectively.

In this work, in order to obtain the averaged pulse profile and to discuss the radiation characteristics of the strong emission phase of PSR B0950 + 08, the emission region of the pulse phase from 0.88–0.92 (see Figs 1 and 2) is regarded as the baseline region and then subtracted. Furthermore, to detect the pulsed radio signal of the 'bridge' emission region of this pulsar, the baseline is subtracted in each single pulse according to the fact that the pulsed radio emission in each individual pulse is narrow. After this, baseline subtraction, i.e. subtracting the receiver contribution, is carried out in each single pulse and the radio emission caused by the systematic contribution is unpulsed. The systematic contribution of the 'bridge' emission region is removed by the impulsive property of the subpulse of this
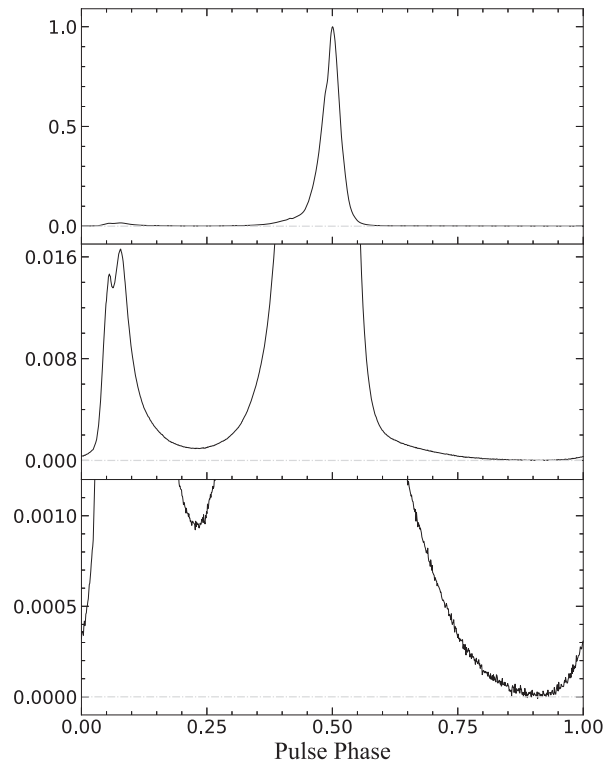
Figure 2. The averaged pulse profile of the whole bandwidth is shown in the top panel, and the corresponding ×60 and ×900 expanded scale views are plotted in the middle and bottom panels, respectively. The emission region of the pulse phase from 0.88−0.92 is regarded as the baseline region.

pulsar. More detailed detection of the pulsed radio signal across the whole pulse phase will be presented in Sections 3 and 4.

3 DATA ANALYSIS AND RADIATION CHARACTERISTICS

In order to discuss the emission characteristics of PSR B0950 + 08, the emission from the 0.17–0.30 and 0.65–0.95 pulse phase intervals shown in Fig. 3, called the low-emission region in the text, is defined as the bridge emission. With this definition, we demonstrate that there is no off-pulse region in the pulse phase of PSR B0950 + 08 in the frequency band 1050–1450 MHz, and the emission, even though in the bridge region, is also impulsive.

The averaged pulse profiles at all remaining frequencies are shown in Fig. 1. As shown in Fig. 1, the radio emission features across the entire pulse longitude are exhibited and the observational properties of the two low-emission regions are clearly revealed from the zoomed-in views in the right panels. The averaged pulse profile of the full bandwidth is also shown in Fig. 2. Apparently, from the figure, there is a concave emission structure rather than a flat platform at the two low-emission regions: the first concave structure appears at a pulse phase of 0.25, meanwhile, another concave structure is revealed at a pulse phase of 0.90. This feature demonstrates a radio-emission behaviour without off-pulse longitude, i.e. the pulsar radiates over the entire pulse period.

To reveal the emission characteristics of the two low-emission regions, a mathematical method is proposed to analyse the emission characteristics of the entire pulse longitude. The Θ(n) function is
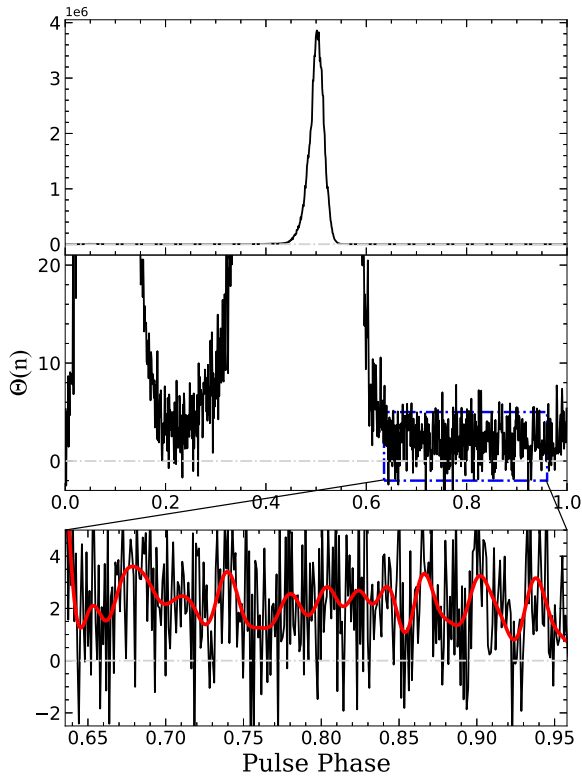
Figure 3. The $\Theta(n)$ function defined in equation (1) for the whole pulse longitude is shown in the top panel, and a vertically zoomed-in view is plotted in the middle panel. Moreover, a detailed view of the region in the dashed-dotted-box is shown in the bottom panel.

defined as the following:

$$\Theta(n) = \sum_{k=1}^{N_{\text{period}}} \left\{ 2 \times \left(I_{k,n-1} - I_{k,n+1}\right)^2 \right.$$
$$\left. - \left[\left(I_{k,n} - I_{k,n-1}\right)^2 + \left(I_{k,n} - I_{k,n+1}\right)^2\right] \right\}, \quad (1)$$

where $I_{k,n}$ represents the signal intensity contributed by the kth pulse and the nth pulse phase bin, and $N_{\text{period}} = 36\,746$ is the number of pulses. The results are shown in Fig. 3.

The $\Theta(n)$ function describes the statistical properties of the radio emission signal. The on-pulse (pulse longitudes that have periodic and impulsive emission) and off-pulse regions can be distinguished by this function, because the value of the $\Theta(n)$ function is positive in on-pulse regions and goes to zero in off-pulse regions (see Appendix A). It should be noted that the fluctuation of the radio emission signals and noise may lead to a statistics error, and this error can possibly be eliminated if the number of individual pulses (N_{period}) is large enough. This statistical property implies that the value of the $\Theta(n)$ function may be influenced by the background noise (discussed in Appendix B). The detailed behaviour of the $\Theta(n)$ function for the entire pulse longitude is illustrated as black curves in Fig. 3, and the detailed properties of the region in dashed-dotted-box in the middle panel are shown in the enlarged bottom panel. From this figure, the result is obviously influenced by background noise in the low-emission region. To determine the emission properties of these regions, the values of the $\Theta(n)$ function in the low-emission region need to be smoothed. The red curve in the bottom panel is the
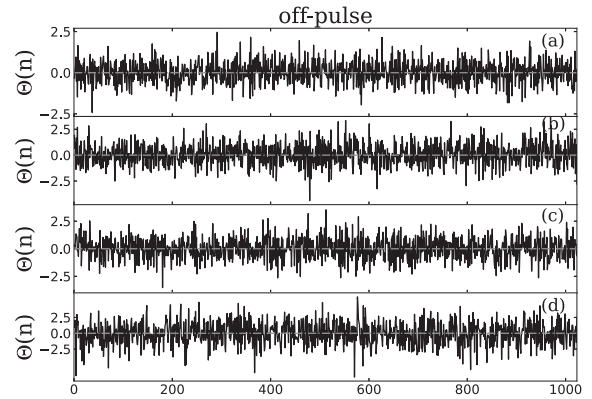
smoothed result achieved via low-pass filtering, and apparently this curve in the low-emission region is greater than zero (dash–dotted grey reference line). It is evident that, in the observed data, the values of the $\Theta(n)$ function in the two low-emission regions are positive. The behaviour of this function illustrates clearly that radio emission signals fill the low-emission region, and this result supports the whole-phase radiation picture that the emission signals fill the entire $360°$ pulse longitude. To demonstrate better that the $\Theta(n)$ function is equal to zero for continuous emission (the unpulsed emission) and is not affected by the non-linear instrumental response, and assuming that the non-linear instrumental response may cause the radio signals of each pulse phase to follow gamma or lognormal distributions, we simulate the $\Theta(n)$-function measurements for those distributions. The behaviour of the $\Theta(n)$ function for these simulations is shown in Fig. 4 to compare with the properties of the $\Theta(n)$ function for the bridge emission region of PSR B0950 + 08. Fig. 4(a), (b), (c), and (d) depict gamma (with shape parameter of 3 and scale parameter of 1), gamma (with shape parameter of 5 and scale parameter of 1), lognormal (with shape parameter of 0.1 and scale parameter of 1), and Gaussian distributions, respectively, and the sample numbers of all simulated data are 10^5. As these figures show, the values of the $\Theta(n)$ function are consistent with zero for continuous emission and the non-linear instrumental response.

Figure 4. Behaviour of the $\Theta(n)$ function for simulated random data. Panels (a) and (b) correspond to gamma distributions with different shape parameters, and panels (c) and (d) represent lognormal and Gaussian distributions, respectively.

4 CONCLUSION AND DISCUSSIONS

In this work, the impulsive emission characteristics of PSR B0950 + 08 are detected for the first time over the whole pulse phase. It is shown that the averaged pulse profile of this pulsar is consistent with previously presented works in the strong emission regions (e.g. Everett & Weisberg 2001; McLaughlin & Rankin 2004; Johnston et al. 2005). From Figs 1, 2, and 3, it is evident that emission in the low-emission region (from pulse phase 0.65–0.95, the emission properties at this pulse longitude are undetected and usually regarded as off-pulse regions in published literature) has been detected for PSR B0950 + 08. With the detection of emission in the bridge regions, the whole-phase radiation characteristics of this pulsar are identified. However, there are some issues that need to be discussed.

The radio emission of PSR B0950 + 08 may originate from the two poles, which is different from the other whole-phase radiation
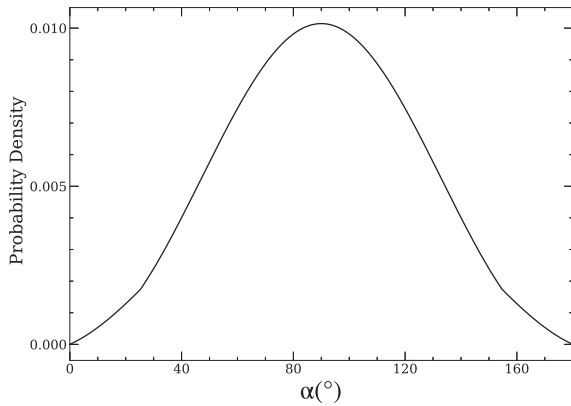
Figure 5. The probability density of magnetic inclination angle α derived from the period and pulse width of PSR B0950 + 08.

pulsar, PSR B0826 − 34. Esamdin et al. (2005) reported that the radiation extends through the whole pulse phase of PSR B0826 − 34 in the 'strong emission mode'. The fact that radio emission signals of PSR B0826 − 34 cover the whole phase could naturally be understandable because the inclination angle, α, is extremely low ($\sim 0.5°$), as is evident from the large pulse width for this pulsar, whereas the pulse width of strong emission for PSR B0950 + 08 is relatively small ($\sim 31.4°$), which implies a large inclination angle. With the assumption of a radiation altitude of 1000 km (at this altitude, the multipole field is weak and the field is dominated by the dipole component), one can calculate the maximum half-width of the radiation beam, θ_μ (corresponding to the radiation from the last open field lines), to be $\sim 25.8°$. Assuming that the directions of the magnetic axis and rotation axis are uniform and ignoring the beam-scale distribution, with equation (2) in Lee et al. (2009) we estimate the probability density of the magnetic inclination angle, α, which is shown in Fig. 5. It can be calculated that the probability density of the inclination angle (smaller that $10°$ or larger than $170°$) is $\sim 2.96 \times 10^{-3}$. Moreover, the inclination angle measured through polarization observation of strong emission is $\alpha \simeq 75°$ (Everett & Weisberg 2001), which implies that the radiation of PSR B0950 + 08 originates from both poles of an almost orthogonal rotator. Therefore, the radio signals of the two bridge regions should be overlapped by radiation from the two poles.

The whole-phase radiation implies that some radio emission from PSR B0950 + 08 must come from high altitude. However, the assumption of a radiation altitude at 1000 km should be discussed carefully. In fact, the mean pulse profile at lower frequency is much wider, with pulse width $\sim 70°$ (Bilous et al. 2022), which suggests that the radiation altitude must be higher than 1500 km under the assumption of $\alpha \simeq 75°$. Furthermore, for the whole-phase radiation, the maximum radiation altitude should be larger than 5000 km even after adjustment for the effects of aberration and retardation. Considering a radius of the light cylinder for PSR B0950 + 08 of $\sim 12\,000$ km and its whole-phase radiation characteristics, there must be a certain pulse longitude at which the emission comes from the two poles at the same time, and it can be derived that the half-width of at least one radiation beam, θ_μ, must not be less than $90°$. According to the radiation altitude equation (see equation 5 in Zhang et al. 2007), we calculate that the emission height of a certain pulse longitude (probably in the two low-emission regions) is larger than ~ 8000 km. With an inclination angle of $75°$, it can also be calculated that, for at least 40 per cent of the entire pulse period, the

radiation comes from an extremely high altitude of 5000 km, which is roughly the altitude of the outer gap where the high-energy emission is thought to originate (Cheng, Ho & Ruderman 1986). However, for the radio radiation of normal pulsars, the radiative particles are supposed to lose energy rapidly and not to keep radiating till reaching such a high altitude (Zhang, Qiao & Han 1997). The radio emission is always regarded as being generated from a low altitude of pulsars, due to two effects: energy loss and the decoherence of the radiative particles which move outwards along the opening magnetic field lines. Radiation altitudes larger that 8000 km challenge the conventional particle acceleration and coherent radiation mechanism in the pulsar magnetosphere discussed in Ruderman & Sutherland (1975), which may imply an additional acceleration electric field over the polar gap, i.e. the slot gap (Arons 1983) or annular gap (Qiao et al. 2007).

The whole-pulse radiation characteristics are unveiled with the $\Theta(n)$ function, which exploits the variation property of the pulsar radiation. In other words, invariant radiation does not affect the analysis results. For example, the stable emission from a pulsar wind nebula which contributes off-pulse emission (Ruan et al. 2020) is different from the whole-phase radiation from a pulsar. In fact, the whole-phase radiation is similar to the non-100-per-cent pulsed fraction radiation of a high-energy pulsar, in which emission occurs over the whole phase while some specific phase regions are preferred.

The physical origin of the radio emission at different pulse longitudes is also noteworthy. The averaged pulse profile shows complex shapes, and its radio emission beam is described by the so-called 'core–cone' model. According to this model, the radio radiation beam consists of a central core surrounded by two rings of nested conal emission, which are respectively named the inner and outer cones (Rankin 1983, 1990). Although the whole-pulse longitude exhibits radio emission, the emission properties vary with different pulse longitudes. In Fig. 2 it can be seen that the well-resolved conal-double structure of the interpulse differs from the unresolved conal-single structure of the main pulse. In Fig. 3, the values of the $\Theta(n)$ function in the two low-emission regions are almost equal to each other, which may indicate similar emission physics.

To determine the emission properties of the bridge regions, the distribution of the radio emission signals at certain pulse longitudes is also considered. This method reveals the emission properties through the distribution of noise and radio emission in each pulse phase bin of the folded data, which follow different statistical laws. Apparently, the fluctuation of noise follows a Gaussian distribution, and this statistical property is different from the lognormal distribution of the radio emission signals of a normal pulse (Cairns, Johnston & Das 2001). This property may mean that the distribution of emission in the on-pulse phase interval is asymmetric. The statistical results are shown in the bottom panel of Fig. 6, and the number of single pulses with fixed radio emission intensity at each pulse phase are represented by different colours. From this figure, there is a small indication that the distribution of the upper and lower of the maximum distribution point (the red points) in each pulse phase bin is asymmetric. To illustrate the asymmetry of the whole-pulse longitudes better, a longitude-resolved test statistic such as the Anderson–Darling test is also used, with the null hypothesis that the distribution of each longitude comes from a Gaussian distribution (Stephens 1974). The Anderson–Darling statistics are shown in the top panel of Fig. 6 as black points and the red points represent the results that are derived from simulated random data with a Gaussian distribution. This demonstrates that the distribution at each longitude deviates from a Gaussian distribution, which is consistent with the distribution
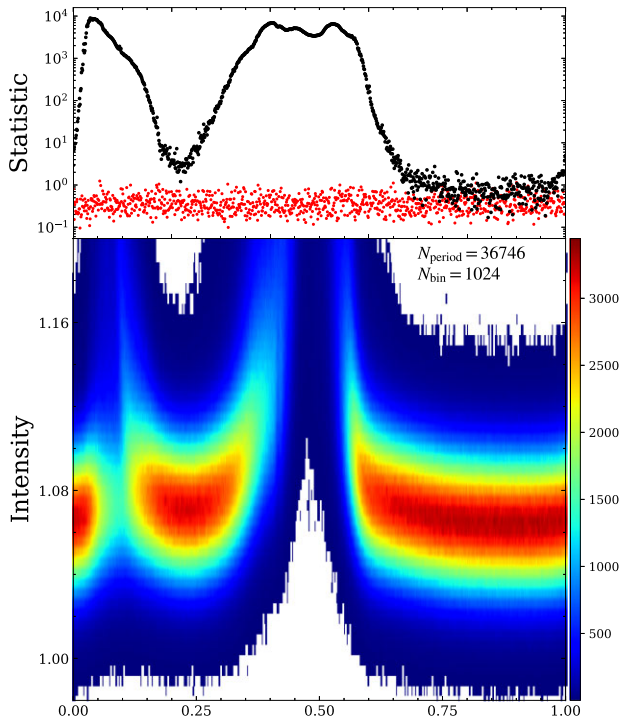
Figure 6. The radio signal distributions at each longitude are shown in the bottom panel, and the top panel shows the statistics of the Anderson–Darling test on them as the black points. The red points are the Anderson–Darling test statistics for simulated random data with a Gaussian distribution. The number of single pulses with fixed radio emission intensity at each pulse phase is represented by different colours.

characteristics in the bottom panel. Although it seems that the above method can also reveal the emission in the bridge regions, the flux distribution in each phase bin may be affected by weak RFI in the frequency domain and the non-linear response of the instrument. In contrast, the $\Theta(n)$ function would be better, since it just refers to radiation variation characteristics in the time domain.

Besides the method used above, the auto-correlation function (ACF) is widely used to reveal the structure characteristics of subpulse and microstructure (Cordes 1976). In this method, we need to use several phase bins (the number of phase bins is usually larger than 10) in each single pulse to calculate the ACF result, and then a conclusion about the existence of radiation in the phase interval of these bins can be drawn. However, it is hard to distinguish whether the radiation exists in a specific pulse phase, due to the relatively long data length to calculate the ACF results. In addition, the ACF may also be influenced by other correlations in the recorded data, i.e. the correlation introduced by the de-dispersion process and the red component of the system noise. In this work, the $\Theta(n)$ function is introduced as a method to judge the existence of radiation in each phase bin. To calculate the $\Theta(n)$ function, the correlation of the intensity evolution (instead of the intensity) between adjacent phase bins is obtained to show the impulsive property of the subpulse. Therefore, the $\Theta(n)$ function represents an intensity correlation of the first order (while the classical ACF method reveals the zero order), which means it avoids being influenced by the inaccuracy of the baseline. In addition, the longitude–longitude cross-correlation can also be used to determine the subpulse width (Karastergiou et al. 2001). However, this method is strongly influenced by the accuracy

of the baseline in each single pulse and would lose efficacy for the weak emission of PSR B0950 + 08.

In this work, the two low-emission regions of the averaged pulse profile for PSR B0950 + 08 exhibit significant concave structure rather than a flat platform, which indicates that there is impulsive radio emission in these two low-emission regions. A $\Theta(n)$ function is proposed to determine the radio signal of the weak emission regions quantitatively. Through data analysis, the $\Theta(n)$ function is found to be a tentative method to determine the radio emission of the bridge regions for this pulsar, because it is based only on the emission correlation of any three adjacent phase bins. However, it should be noted that, given the time-scale discussed in Appendix A, the $\Theta(n)$ function may not be suitable for detecting the radiation of all pulsars. One should be cautious in applying the $\Theta(n)$ function to determine the radio signal in the weak emission regions of other pulsars.

It is difficult to determine the baseline position of PSR B0950 + 08, because the baseline determination for this pulsar is affected by many problems. For instance, conventional baseline subtraction is not suitable for this pulsar. Secondly, the change of the baseline with time will affect its determination. Moreover, the radiation intensity of this pulsar is influenced by the effect of interstellar scintillation (e.g. Bilous et al. 2022), which could also influence the determination process. In fact, the baseline emission is much more difficult to remove completely for a single-dish radio telescope. In this work, the detection result of the $\Theta(n)$ function is hardly affected by the baseline emission of PSR B0950 + 08 for this observation, since it depends only on the pulsed radio signal of the subpulse of this pulsar. The baseline emission of the pulsar can be determined by the radio interferometer through analysing the spatial variation of the background emission. More precise measurements for the baseline emission of this pulsar may be provided by future interferometers such as the Square Kilometers Array (SKA) (Carilli 2015) or the FAST extension array (FASTA).

Determination of the accuracy baseline is very important for pulsars with detectable emission over the whole pulse phase, since the PPA is related to the radiation geometry. However, the PPA of the whole-phase radiation is hard to calibrate, because it is sensitive to the baseline determination in the weak radiation phase region. The polarization features of this pulsar are not presented in this work, since we have not made a satisfactory calibration during the observations. The non-linear evolution of the baseline response with time severely influenced the calibration. Therefore, real-time calibration information is needed to determine the baselines of the Stokes parameters precisely, and the optimized calibration of this pulsar has already been planned.

The effects of saturation from the digitization process are presented in Jenet & Anderson (1998). There will be an artefact caused by the analogue-to-digital conversion and dispersion, which may bring scattered power into the data. This effect will result in a fake correlation along the pulse phase and a wider radiation phase, and the range of this effect depends on the dispersion. We calculated that the dispersion sweep in our frequency range of 1050–1450 MHz is 5.3 ms, ~ 2 per cent of the entire pulse period for PSR B0950 + 08. Thus, with the digitization effect, the radio pulse would be widened by 2 per cent and an artificial correlation within 2 per cent of the pulse period would be produced. The non-zero value of the $\Theta(n)$ function may be also induced by time correlation. We expect that future interferometers such as SKA or FASTA will verify the current findings. Additionally, we anticipate that FAST and these future interferometers will potentially detect more pulsars with whole-phase radiation in the future.

DATA AVAILABILITY

The data underlying this work are available in the FAST project PT2020 − 0034, and can be shared on request to the FAST Data Center.

REFERENCES

Arons J., 1983, ApJ, 266, 215
Bilous A. V. et al., 2022, A&A, 658, A143
Cairns I. H., 2004, ApJ, 610, 948
Cairns I. H., Johnston S., Das P., 2001, ApJ, 563, L65
Carilli C., 2015, in Proceedings of Advancing Astrophysics with the Square Kilometre Array (AASKA14), Giardini Naxos, Italy, p. 171, preprint (arXiv:1408.5317)
Cheng K. S., Ho C., Ruderman M., 1986, ApJ, 300, 500
Cordes J. M., 1976, ApJ, 208, 944
Dai S. et al., 2015, MNRAS, 449, 3223
Esamdin A., Lyne A. G., Graham-Smith F., Kramer M., Manchester R. N., Wu X., 2005, MNRAS, 356, 59
Everett J. E., Weisberg J. M., 2001, ApJ, 553, 341
Hankins T. H., Cordes J. M., 1981, ApJ, 249, 241
Hankins T. H., Izvekova V. A., Malofeev V. M., Rankin J. M., Shitov Y. P., Stinebring D. R., 1991, ApJ, 373, L17
Hobbs G., Lyne A. G., Kramer M., Martin C. E., Jordan C., 2004, MNRAS, 353, 1311
Hotan A. W., van Straten W., Manchester R. N., 2004, PASA, 21, 302
Jenet F. A., Anderson S. B., 1998, PASP, 110, 1467
Jiang P. et al., 2019, Science China Physics, Mechanics, and Astronomy, 62, 959502
Jiang P. et al., 2020, Research in Astronomy and Astrophysics, 20, 064
Johnston S., Hobbs G., Vigeland S., Kramer M., Weisberg J. M., Lyne A. G., 2005, MNRAS, 364, 1397
Karastergiou A. et al., 2001, A&A, 379, 270
Kuzmin A. D., Izvekova V. A., Shitov Y. P., Sieber W., Jessner A., Wielebinski R., Lyne A. G., Smith F. G., 1998, A&AS, 127, 355
Lee K. J., Cui X. H., Wang H. G., Qiao G. J., Xu R. X., 2009, ApJ, 703, 507
Lu J. et al., 2019, Science China Physics, Mechanics, and Astronomy, 62, 959505
Marcote B., Maan Y., Paragi Z., Keimpema A., 2019, A&A, 627, L2
McLaughlin M. A., Rankin J. M., 2004, MNRAS, 351, 808
Navarro J., de Bruyn A. G., Frail D. A., Kulkarni S. R., Lyne A. G., 1995, ApJ, 455, L55
Nowakowski L. A., Bhat N. D. R., Lorimer D. R., 2002, Proceedings of the conference American Astronomical Society, 34, 1297
Popov M. V., Bartel N., Cannon W. H., Novikov A. Y., Kondratiev V. I., Altunin V. I., 2002, A&A, 396, 171
Qiao G.-J., Lee K.-J., Zhang B., Wang H.-G., Xu R.-X., 2007, Chinese J. Astron. Astrophys., 7, 496
Radhakrishnan V., Cooke D. J., 1969, Astrophys. Lett., 3, 225
Rankin J. M., 1983, ApJ, 274, 333
Rankin J. M., 1990, ApJ, 352, 247
Ruan D., Taylor G. B., Dowell J., Stovall K., Schinzel F. K., Demorest P. B., 2020, MNRAS, 495, 2125
Ruderman M. A., Sutherland P. G., 1975, ApJ, 196, 51
Shabanova T. V., Shitov Y. P., 2004, A&A, 418, 203
Singal A. K., Vats H. O., 2012, AJ, 144, 155
Stephens M. A., 1974, Journal of the American Statistical Association, 69, 730
Tsai J.-W. et al., 2015, AJ, 149, 65
Ulyanov O. M., Skoryk A. O., Shevtsova A. I., Plakhov M. S., Ulyanova O. O., 2016, MNRAS, 455, 150
van Straten W., Bailes M., 2011, PASA, 28, 1
Xu R., 2021, National Science Review, 8, nwab204
Zhang B., Qiao G. J., Han J. L., 1997, ApJ, 491, 891
Zhang H., Qiao G. J., Han J. L., Lee K. J., Wang H. G., 2007, A&A, 465, 525

APPENDIX A: THE PROPERTIES OF THE Θ FUNCTION

The detailed expression for the $\Theta(n)$ function is shown in equation (1); here we will present evidence that the values of the $\Theta(n)$ function in the emission regions are positive.

For the data, in any pulse phase interval with emission, the intensity of the noise follows a Gaussian distribution. The properties of the $\Theta(n)$ function can be described as follows:

$$
\begin{aligned}
\Theta(n) &= \sum_{k=1}^{N_{\text{period}}} \left\{ 2\left(I_{k,n-1} - I_{k,n+1}\right)^2 \right. \\
&\quad \left. - \left[\left(I_{k,n-1} - I_{k,n}\right)^2 + \left(I_{k,n} - I_{k,n+1}\right)^2\right] \right\} \\
&= \sum_{k=1}^{N_{\text{period}}} \left\{ 2\left(S_{k,n-1} - S_{k,n+1} + \sigma_{k,n-1} - \sigma_{k,n+1}\right)^2 \right. \\
&\quad - \left[\left(S_{k,n-1} - S_{k,n} + \sigma_{k,n-1} - \sigma_{k,n}\right)^2\right] \\
&\quad \left. - \left[\left(S_{k,n+1} - S_{k,n} + \sigma_{k,n+1} - \sigma_{k,n}\right)^2\right] \right\} \\
&\approx \sum_{k=1}^{N_{\text{period}}} \left\{ 2\left(S_{k,n-1} - S_{k,n+1}\right)^2 \right. \\
&\quad \left. - \left[\left(S_{k,n-1} - S_{k,n}\right)^2 + \left(S_{k,n} - S_{k,n+1}\right)^2\right] \right\},
\end{aligned} \tag{A1}
$$

where $S_{k,n}$ and $\sigma_{k,n}$ are the emission signal and noise intensity contributed by the kth pulse and nth pulse phase bin, respectively.

For the observation data, the same structure of subpulse repeats many times over a large number of cycles, so that pulse phase is ergodic in all positions of the subpulse. In other words, the summation of all cycles is equivalent to that of all points in subpulses with different shapes,

$$
\begin{aligned}
\Theta(n) &\approx \sum_{k=1}^{N_{\text{period}}} \frac{1}{L} \sum_{l=1}^{L} \left\{ 2\left(S_{k,n,l-1} - S_{k,n,l+1}\right)^2 \right. \\
&\quad \left. - \left[\left(S_{k,n,l} - S_{k,n,l-1}\right)^2 + \left(S_{k,n,l} - S_{k,n,l+1}\right)^2\right] \right\} \\
&\approx \sum_{k=1}^{N_{\text{period}}} \frac{1}{L} \sum_{l=1}^{L} \left\{ \left(S_{k,n,l} - S_{k,n,l-1}\right)^2 + \left(S_{k,n,l+1} - S_{k,n,l}\right)^2 \right. \\
&\quad \left. + 4\left(S_{k,n,l} - S_{k,n,l-1}\right)\left(S_{k,n,l+1} - S_{k,n,l}\right) \right\} \\
&\approx \sum_{k=1}^{N_{\text{period}}} \frac{1}{L} \sum_{l=1}^{L} \left(\Delta_l^2 + \Delta_{l-1}^2 + 4\Delta_l \Delta_{l-1}\right)
\end{aligned} \tag{A2}
$$

where $S_{k,n,l}$ is the lth bin of the subpulse with L bins of the kth pulse and nth pulse phase bin and $\Delta_l = S_{k,n,l+1} - S_{k,n,l}$ is the first-order difference of the subpulse.

In this work, the time resolution of the folded data is ~ 0.25 ms. According to the previous work, the characteristics time-scale of the fine structure is ~ 1 ms for PSR B0950 + 08 (Ulyanov et al. 2016). In other words, the second-order difference can scarcely change sign in succession in 1 ms (~ 4 phase bins) for the folded data. In the interval in which the second-order difference has the same sign (the bin indices of the start and end of the interval are l_s and l_e, respectively), Δ_l is monotonic. Fig. A1 shows an example of the profile shape and its differences at first and second order in the top, middle, and bottom panels, respectively; the vertical dot–dashed lines in the figure divide the profile into several segments. It can be seen that the second-order difference in each segment has the same sign and the first-order difference is monotonic. If the sign of Δ_l does not change, we have $M = \sum_{l=l_s}^{l_e}\left(\Delta_l^2 + \Delta_{l-1}^2 + 4\Delta_l\Delta_{l-1}\right) \geq 0$.

Otherwise, if Δ_l changes sign, without loss of generality, supposing $\Delta_{l_s} \geq ... \geq \Delta_m > 0 \geq \Delta_{m+1} \geq ... \geq \Delta_{l_e}$, it follows that

$$
\begin{aligned}
&\sum_{l_s}^{l_e}\left(\Delta_l^2 + \Delta_{l-1}^2 + 4\Delta_l\Delta_{l-1}\right) \\
&= \sum_{l=m-1}^{l_s}\left(\Delta_l^2 + \Delta_{l-1}^2 + 4\Delta_l\Delta_{l-1}\right) + \left(\Delta_m^2 + \Delta_{m-1}^2 + 4\Delta_m\Delta_{m-1}\right) \\
&\quad + \left(\Delta_{m+1}^2 + \Delta_m^2 + 4\Delta_{m+1}\Delta_m\right) + \sum_{l=m+2}^{l_e}\left(\Delta_l^2 + \Delta_{l-1}^2 + 4\Delta_l\Delta_{l-1}\right) \\
&\geq \left(\Delta_m^2 + \Delta_{m-1}^2 + 4\Delta_m\Delta_{m-1}\right) + \left(\Delta_{m+1}^2 + \Delta_m^2 + 4\Delta_{m+1}\Delta_m\right) \\
&= \Delta_{m-1}^2 - 2\Delta_m^2 + 4\Delta_m\Delta_{m-1} + (\Delta_{m+1} + 2\Delta_m)^2 \\
&\geq \Delta_{m-1}^2 - 2\Delta_m^2 + 4\Delta_m\Delta_{m-1} \\
&\geq \Delta_m^2 - 2\Delta_m^2 + 4\Delta_m^2 \\
&= 3\Delta_m^2 > 0. \quad\quad\quad\quad\quad\quad\quad\quad\quad\quad\quad (A3)
\end{aligned}
$$

To sum up, $\Theta(n) > 0$ during the interval of the emission pulse phase.
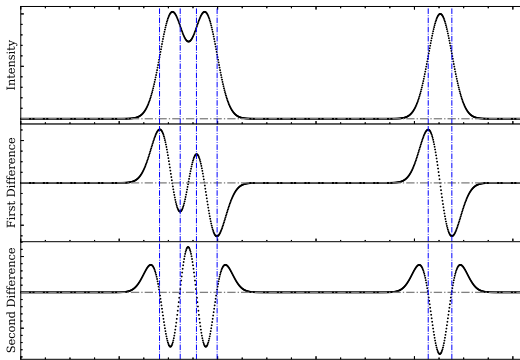

Figure A1. Intensity profile shape and its differences; the dot–dashed grey line represents the reference zero line. The vertical dot–dashed lines divide the profile into several segments based on the sign of the second-order difference.
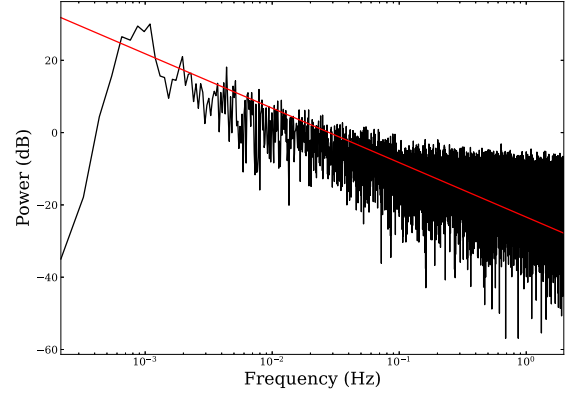

Figure B1. The spectrum of the background-noise intensity is normalized by its white-noise intensity; the red line corresponds to the power-law fitting. The background noise intensity is obtained by averaging the minimum 10 phase bins in each period.
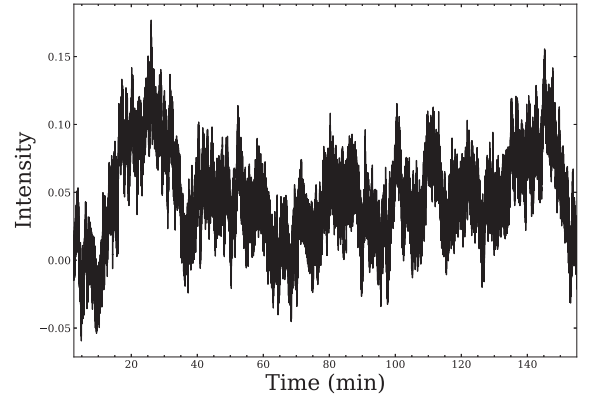

Figure B2. Simulated noise according to the power law $P(f) = 3.969 \times 10^{-3}f^{-1.506}$, which has the same white-noise intensity as the background noise.

APPENDIX B: THE EFFECTS OF BACKGROUND NOISE

When using the $\Theta(n)$ function to determine quantitatively the emission characteristics of the weak regions, such as the two low-emission regions of PSR B0950 + 08 in this work, one concern is the effects of background noise, particularly the red-noise components. Fig. B1 shows the spectrum of the background-noise intensity relative to white noise; the red line corresponds to the power-law fitting of the red-noise component, $P(f) = 3.969 \times 10^{-3}f^{-1.506}$. With the power-law expression, the background noise, which has the same white-noise intensity as the observed data, is simulated. The simulated red noise is shown in Fig. B2. The value of the $\Theta(n)$ function of the simulated noise is calculated and presented in Fig. B3(a). In addition, for comparison, the $\Theta(n)$ function of the pure red-noise component is shown in Fig. B3(b). It can be seen that the positive property of the $\Theta(n)$ function is scarcely affected by the red-noise components in this observation, and the fluctuations of the $\Theta(n)$ function in Fig. 3 almost all result from the background noise.
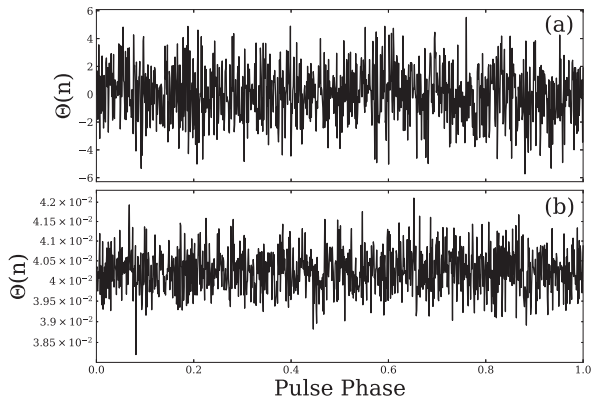
Figure B3. The $\Theta(n)$ function of the simulated background noise and its red-noise components are shown in panels (a) and (b), respectively.

This paper has been typeset from a TEX/LATEX file prepared by the author.